Icarus 325 (2019) 94–104

Contents lists available at ScienceDirect

Icarus

journal homepage: www.elsevier.com/locate/icarus

Decimeter-scale particle characterization in the coma of 73P/Schwassmann-Wachmann 3 using dual-wavelength radar observations

A. Virkki[a,*], E. Zubko[b], M.C. Nolan[c], E.S. Howell[c], L.A.M. Benner[d], J.K. Harmon[a,1]

[a] Arecibo Observatory, University of Central Florida, HC-3 Box 53995, Arecibo, 00612, Puerto Rico
[b] School of Natural Sciences, Far Eastern Federal University, 8 Sukhanova St., Vladivostok, 690950, Russia
[c] Lunar and Planetary Laboratory, University of Arizona, PO Box 210092, Tucson, AZ 85721-0092, USA
[d] Jet Propulsion Laboratory, California Institute of Technology, 4800 Oak Grove Drive, Pasadena, CA 91109, USA

ARTICLE INFO

Keywords:
Radar observations
Comets
Coma
73P

ABSTRACT

We investigate the centimeter-to-decimeter-scale particle size distribution and dynamics in the coma of Comet 73P/Schwassmann-Wachmann 3 using radar observations obtained shortly after the comet's disintegration in May 2006. We derive the particle size distribution power-law index in the comae of fragments B and C using radar cross sections and circular-polarization ratios observed at S and X bands (2.38 GHz and 8.56 GHz, respectively), and show day-to-day changes in the number of contributing particles. We test three irregular particle morphologies, but find that the particle shape plays a relatively minor role. The power-law indices from 4.0 to 4.8 and major-axis diameters up to about 30 cm provide the best fits to the radar observations, the values depending on the particle shape and the observed radial velocity. A majority of the measured particle velocities exceed the escape velocity of the nuclei.

1. Introduction

The first comet for which planetary radar observations gave evidence of decimeter-scale particles in the coma was C/Iras-Araki-Alcock in 1983 (Harmon et al., 1989). To date, centimeter-to-meter scale particles have been detected in less than half of all radar-observed comets but, when present, they can account for a significant fraction of the mass loss (Harmon et al., 2004). One of the brightest comae that has been detected using planetary radar is the coma of 73P/Schwassmann-Wachmann 3.

73P is a periodic comet that was discovered by Arnold Schwassmann and Arno Arthur Wachmann in 1930. 73P began to disintegrate in 1995 and broke further into several fragments in 2006 (Fig. 1) as a result of returning to the inner Solar System (Weaver et al., 2006). We obtained observations of the largest fragments B and C using the Arecibo Observatory's S-band radar system and the Goldstone Observatory's X-band radar system in May, 2006; fragment G was attempted but not detected (Nolan et al., 2006). The diameter of fragment B was estimated to be 400-800 m, and the diameter of fragment C 1–2 km (Howell et al., 2007).

The coma particle size distribution (PSD) follows a power-law function: $n(r) \propto r^{-\nu}$. For example, Reach et al. (2009) have determined size distributions for large (10–100-m-scale) particles in the comae of 73P fragments B and C based on the cumulative luminosity distribution: $\nu = 1.84$ for particles with flux < 10 mJy and $\nu = 2.56$ for particles with flux > 10 mJy. Absolute particle size for 10 mJy is not given but it is roughly in the size scale of 50 m.

For other comets, Mazets et al. (1986) show that the power-law index ν spans the range from 1.5 to 3 as detected *in situ* in submicron- and micron-sized dust particles in comet 1P/Halley. They also demonstrate the power-law index to increase with the particle size, e.g., to 3.4 in super-micron particles. Laboratory analysis of micron-sized craters in aluminum foil exposed in the vicinity of the nucleus of comet 81P/Wild 2 suggests a power-law index of $\nu = 2.89$ in its coma particles in the size range from 0.1 μm to 10 μm (Price et al., 2010), which is consistent with the findings by Mazets et al. (1986). Furthermore, the Stardust findings in comet 81P/Wild 2 also suggest that the power-law index increases with particle size (Tuzzolino et al., 2004). Hilchenbach et al. (2016) find a power-law index $\nu = 3.1$ for coma grains from 14 μm to sub-millimeter scale for 67P/Churyumov-Gerasimenko, while Kelley et al. (2008) report a value as large as $\nu = 3.5$ for grain sizes from 1 to 100 μm. Studies based on Rosetta's Grain Impact Analyzer and Dust Accumulator (GIADA) instrument and OSIRIS cameras report $\nu = 4$ for dust particles greater than 1 mm in the coma of 67P (Fulle

* Corresponding author.
E-mail address: avirkki@naic.edu (A. Virkki).
[1] Retired.

https://doi.org/10.1016/j.icarus.2019.02.009
Received 22 August 2018; Received in revised form 25 January 2019; Accepted 11 February 2019
Available online 18 February 2019
0019-1035/

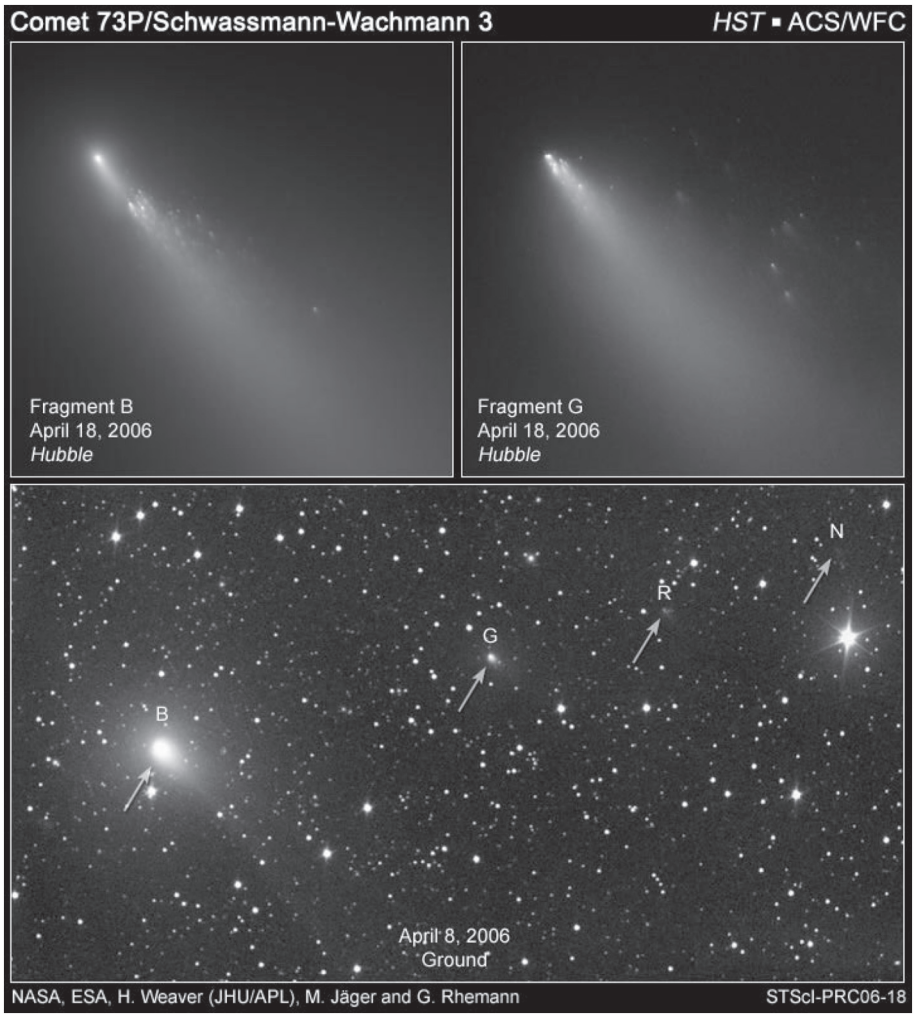

Fig. 1. The fragmented comet 73P as seen by optical observation in April 2006.

et al., 2016b).

As Mazets et al. (1986) and Kelley et al. (2008) point out, a single power-law size distribution may not represent the whole PSD of a cometary coma well, but it serves as a good approximation over a limited range. The observed PSD can be different from the ejected PSD, as primarily the large grains accumulate over time. In terms of radar, which only detects the chunks of ice detached from the nucleus, there may not be a significant difference between the observed and ejected PSD, but it should be taken into account when considering the full size distribution of the coma.

In this paper, we present numerical modeling of radar scattering of large coma particles. We consider the particle size distribution, maximum particle size, and the particle shape. We selected the comet 73P/Schwassmann-Wachmann 3 as an application to the modeling work, because it is one of the few comets for which a coma has been detected in both S-band and X-band radar observations. We show that multi-wavelength observations are critical for constraining the coma particle size distribution.

In Section 2, we review the basics of radar observations and present the detected radar properties of 73P. In Section 3, we present the methodology in detail, the parameters we chose for the numerical modeling work, and show how the radar observables depend on their physical parameters. In Section 4, we present the modeling results and discuss how the coma particle size distribution and velocity change as a function of distance from the nucleus and estimate the daily variation in the number of contributing particles.

2. Observations

We observed 73P/Schwassmann-Wachmann 3 in a similar way as other common radar observations of asteroids and comets: the radar system transmits a powerful circularly polarized signal, and detects the echo simultaneously in the same circular (SC) and the opposite circular (OC) polarization as compared to the transmitted signal (Ostro, 1993). Radar detection of a coma is determined by the abundance of particles larger than the Rayleigh limit $\lambda/2\pi$ (where λ is the wavelength). The echo power in the OC polarization is typically 5–10 times stronger than in the SC polarization (Harmon et al., 2004).

The planetary radar system at the Arecibo Observatory used the 305-m William E. Gordon radio telescope, transmit power of 670–868 kW, and a wavelength of 12.6 cm (2.38 GHz, S band), and at the Goldstone Observatory a 70-m DSS-14 radio telescope, transmit power of 425 kW and a wavelength of 3.55 cm (8.56 GHz, X band). For further information on the technical capabilities of each system, see Naidu et al. (2016).

The Doppler spectra measurements, often referred to as “continuous wave” (CW), provide the radar cross section:

$$\sigma = \frac{(4\pi)^3 d^4 P_{rx}}{G_A^2 \lambda^2 P_{tx}}, \tag{1}$$

where d is the target's distance from the observer, P_{tx} and P_{rx} are the transmitted and received power, respectively, and G_A is the telescope gain, or $4\pi/\lambda^2$ times the effective aperture of the antenna (Ostro, 1993).

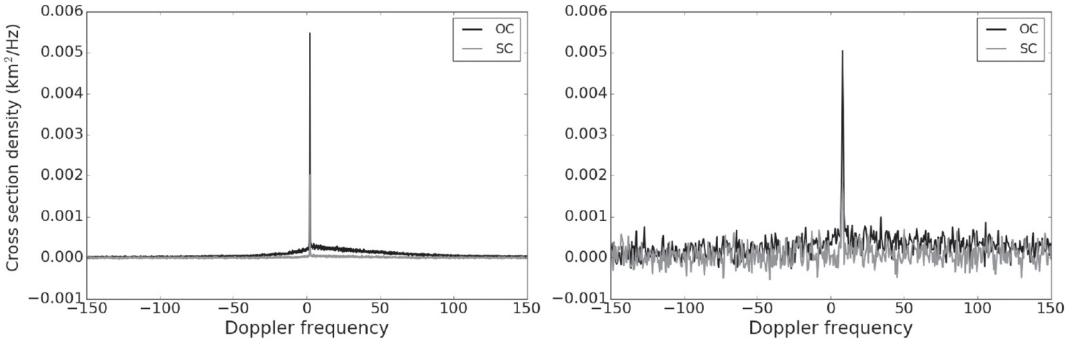

Fig. 2. The Doppler spectrum (radar cross section density per Doppler frequency) of 73P/SW3-B on May 14, 2006, in the opposite circular (OC, black) and same circular (SC, gray) polarization as observed using the S-band planetary radar system at the Arecibo Observatory (on the left) or the X-band planetary radar system at the Goldstone Observatory (on the right), the nucleus included (the peak in the middle).

The radar cross section in the SC polarization divided by that in the OC polarization gives the polarization ratio:

$$\mu_C = \frac{\sigma_{SC}}{\sigma_{OC}}. \quad (2)$$

The systematic uncertainty is about 25% for the radar cross sections and only about 5% for the circular polarization ratios as errors due to, e.g., the antenna gain cancel out in the division.

We measure the Doppler shift with respect to the nucleus so that the expected Doppler shift of the center of mass of the nucleus as given by the ephemeris is zero. The nucleus is seen in the Doppler spectra as a narrow peak with the coma seen as a broad "skirt" echo extending to several hundreds of Hertz around the nucleus (Fig. 2). Although the coma echo is much broader than the nucleus echo, it contributes less than 10% of the total echo power. The observed Doppler bandwidth of the nucleus is determined by the size and the spin period of the nucleus, whereas the Doppler shift of the coma particles is primarily due to the particle motion towards or away from the observer rather than their rotation. The coma echoes for each day (nucleus removed) are displayed in Fig. 3, illustrating the change in the shape and strength of the coma skirt echo as the Sun-comet-Earth geometry evolves.

The detected radar quantities of comae of fragments B and C are listed in Table 1. Fragment C was observed before and after the day of the closest Earth-approach, May 12, while all the detections of fragment B are after this day and extend a few days beyond those of fragment C. The observations of fragment C show an increasing trend of radar cross sections in both the OC and SC polarizations as a function of time, which implies increase in the number of large particles in the coma. In contrast, fragment B shows a decreasing trend of the same parameters during the days it was observed.

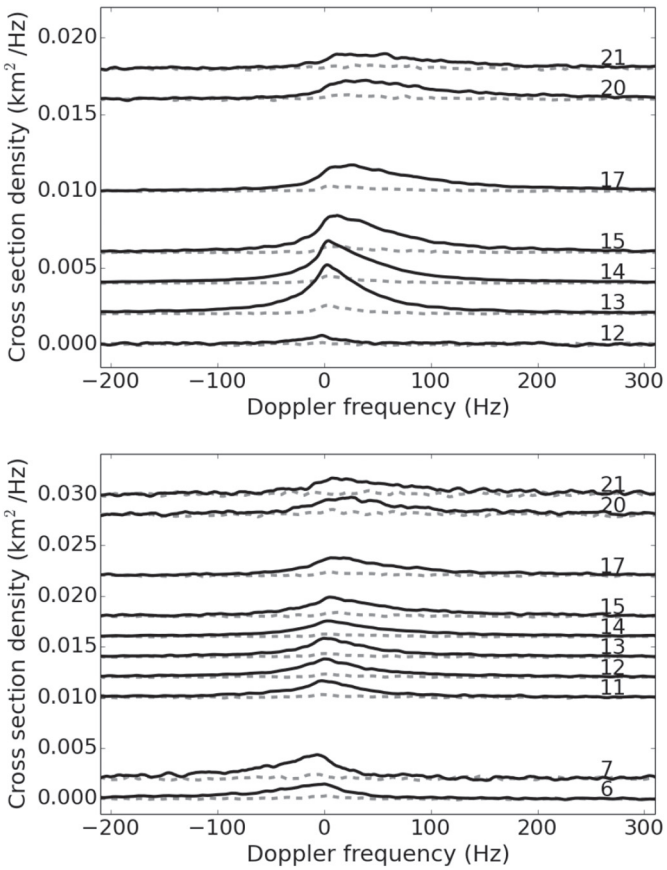

Fig. 3. The Doppler spectra of 73P/SW3-B (on the top) and 73P/SW3-C (on the bottom) on each observation day in May 2006, as labeled in the image, smoothed to 10 Hz and the nucleus removed, including a vertical offset based on the observation date and a horizontal offset to center the Doppler shift of the nucleus to 0 Hz. The OC polarization is displayed as black solid lines and the SC polarization as gray dashed lines. All spectra in these panels are measured using the Arecibo Observatory S-band planetary radar system.

3. Numerical modeling

So far, only one space mission, Stardust, has returned a sample of cometary dust on its visit to 81P/Wild 2 (Brownlee et al., 2006). These particles, as well as the cometary dust particles collected by Rosetta's COSIMA instrument (Langevin et al., 2016), and those in the Earth's stratosphere by high-altitude airplanes (e.g., Busemann et al., 2009), are typically less than a millimeter in size. Despite missions such as Stardust or Rosetta, which have increased our understanding of comets remarkably, there remains a question of how representative the few sampled comets are out of the thousands, especially when we study *in situ* only short-period comets. Numerical modeling of electromagnetic scattering is a cost-effective way to study the physical properties of nuclei as well as comae of both short- and long-period comets.

The radar echo of a target depends on three physical parameters of the scattering particles: the electric permittivity, the shape, and the size relative to the wavelength of the incident signal. In Section 3.1, we describe three different particle shape categories considered in this study, in Section 3.2, we address the selected range of sizes and size distributions, and in Section 3.3, we discuss our assumptions for realistic electric permittivities. In Section 3.4 we provide a detailed description of the methodology of how we derive the optimal power-law index and maximum particle size from dual-wavelength observations. The method has some similarities to that presented by Harmon et al. (1989), but we use more realistic particle shapes and consider a wider range of both power-law indices and particle sizes.

Also, we consider the what role the distance from the nucleus plays in the coma particle properties. Howell et al. (2007) report a size-

Table 1
The observed radar scattering properties for the coma of 73P fragments B and C. The first column gives the designation of the fragment. The second column gives the observation date in 2006. The third column designates the observatory (A for Arecibo, G for Goldstone). The fourth and fifth columns give the detected total radar cross section in km^2 in OC and SC polarization, respectively. The sixth column gives the total circular polarization ratio (Eq. (2)). The seventh and eighth columns show the target's distance from the observer in astronomical units (note the different locations of the telescopes observing fragment B on May 14), and the Sun-target-observer angle in degrees at 12:00 UT. Listed uncertainties include 1–4% of error based on noise statistics, the dominating systematic uncertainties of 25% for the radar cross sections, and systematic uncertainties of 5% for the polarization ratios. May 12 for fragment B is omitted due to a larger systematic uncertainty.

Target	Date	Loc.	$\sigma_{OC} \pm \delta\sigma_{OC}$	$\sigma_{SC} \pm \delta\sigma_{SC}$	$\mu_C \pm \delta\mu_C$	d (au)	S-T-O (°)
C	May 06	A	0.196 ± 0.049	0.017 ± 0.005	0.085 ± 0.018	0.0937	64.809
C	May 07	A	0.283 ± 0.071	0.014 ± 0.007	0.050 ± 0.023	0.0893	68.090
C	May 11	A	0.193 ± 0.048	0.017 ± 0.005	0.090 ± 0.015	0.0790	83.525
C	May 12	A	0.210 ± 0.053	0.021 ± 0.006	0.101 ± 0.012	0.0786	87.597
C	May 13	A	0.204 ± 0.051	0.015 ± 0.004	0.074 ± 0.012	0.0791	91.526
C	May 14	A	0.206 ± 0.052	0.019 ± 0.005	0.094 ± 0.014	0.0806	95.193
C	May 15	A	0.251 ± 0.063	0.017 ± 0.005	0.069 ± 0.015	0.0829	98.501
C	May 17	A	0.262 ± 0.066	0.027 ± 0.007	0.104 ± 0.015	0.0899	103.825
B	May 13	A	0.309 ± 0.077	0.025 ± 0.007	0.079 ± 0.010	0.0672	88.245
B	May 14	A	0.272 ± 0.068	0.023 ± 0.006	0.084 ± 0.004	0.0669	92.918
B	May 14	G	0.309 ± 0.078	0.086 ± 0.026	0.279 ± 0.052	0.0669	92.941
B	May 15	A	0.296 ± 0.074	0.022 ± 0.006	0.074 ± 0.010	0.0677	97.350
B	May 17	A	0.249 ± 0.062	0.024 ± 0.006	0.097 ± 0.010	0.0722	104.840
B	May 20	A	0.214 ± 0.054	0.022 ± 0.007	0.101 ± 0.018	0.0849	111.706
B	May 21	A	0.155 ± 0.039	0.017 ± 0.006	0.112 ± 0.027	0.0904	112.930

dependency of the particle velocities; smaller particles have greater velocities than larger particles, which is also consistent with the analysis by Reach et al. (2009): The sublimation of volatiles ("rocket forces"), solar radiation pressure, and gravitational forces can act as accelerating forces, but the acceleration due to gas ejection and solar radiation affect smaller particles more strongly, whereas the speed of large particles is dominated by the ejection speed during fragmentation. Therefore, the particle size distribution properties can be expected to change as a function of distance from the nucleus.

3.1. Shape

The particle shape, surface roughness, and packing density can have a significant impact on the circular polarization in the backscattering direction (Zubko et al., 2007, 2008; Kemppinen et al., 2015; Virkki and Muinonen, 2016). The morphology of micron-sized dust particles collected by Stardust in comet 81P/Wild 2 or those detected by Rosetta's GIADA and OSIRIS instruments should not necessarily appear in centimeter- and decimeter-sized chunks. Because there is no physical evidence of the morphology of the decimeter-scale particles, we consider it critical to test different morphologies to provide a demonstration of the role that the particle shape plays in radar scattering.

The most realistic morphologies are irregular but compact. For this paper, we chose three different shape categories (Fig. 4). The first category are natural atmospheric dust (ND) particle shapes. Their surface roughness is greater than that of the other selected morphologies, which is useful for considering the effect of the particles' surface roughness on the observed radar parameters. The shapes were laboratory-characterized using a scanning electron microscope as reported by Lindqvist et al. (2014). This category only includes two particles as detected in more than 2500 orientations. The small number of sample particles could lead to scattering profile features that are specific to certain geometric features of the particles but averaging the scattering profile over a large number of orientations mitigates that risk.

As a second category, we utilize Gaussian-random-sphere (GRS) particles (Muinonen et al., 1996; Zubko et al., 2007), which allow a fast generation of relatively stochastic but compact shapes. We generated 100 test particles using a standard deviation of radius $\delta = 0.245$ and a power-law index $\nu_{cov} = 4$ for the covariance function that determines the variance of the shape. For more details on light-scattering computations of GRS particles and verification of statistical reliability of the obtained results, see Zubko et al. (2007).

For a third category, we chose agglomerated debris (AD) particles, which are in appearance the least compact of the three categories, but could be considered as compact smaller particles agglomerated together. A significant advantage of the agglomerated debris particles is that in smaller size scales they are capable of reproducing the degree of linear polarization and phase function over wide range of phase angles, photometric and polarimetric color measured at visible wavelengths in numerous comets (Zubko et al., 2016). AD particles are consistent with

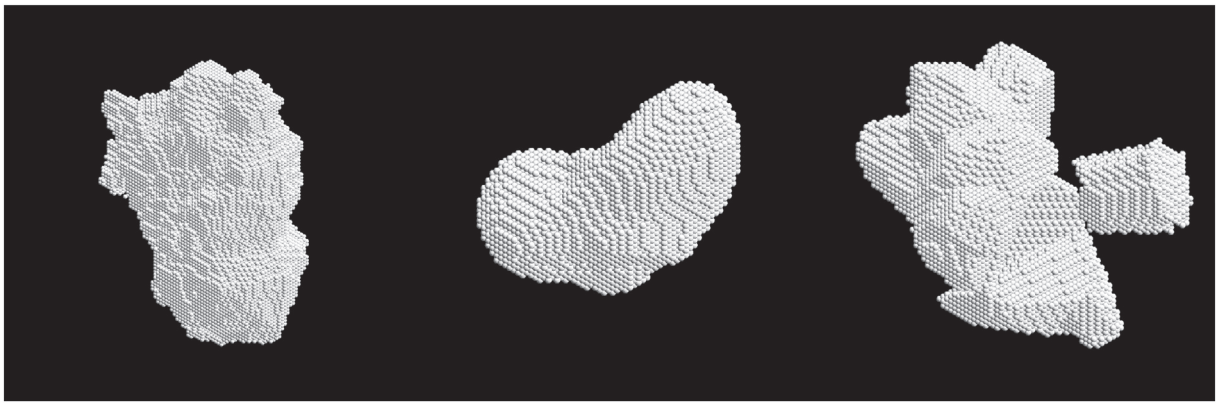

Fig. 4. Examples of the model particles: On the left, a natural dust (ND) particle, in the middle, a Gaussian-random-sphere (GRS) particle, and on the right, an agglomerated debris (AD) particle.

Table 2
A summary of the sample particle parameters. The first column shows the particle type, the second column shows the number of particles of each type, and the third column gives the number of orientation over which the scattering by each particle type was considered.

Particle	Sample size	Orientations
ND	2	2592
GRS	100	5–6
AD	500	1

literature on cometary micron-sized dust, and it is possible that the chunks detached from the nucleus could preserve their relatively high bulk material density, 0.6–1 g/cm^3. In this work we average light-scattering response over a minimum of 500 different shapes of the AD particles with an average packing density of 0.236. More details on the generation algorithm for the AD particles, and numerical simulation of their light-scattering response can be found, e.g., in Zubko et al. (2015).

We utilize a discrete-dipole approximation code ADDA (Yurkin and Hoekstra, 2011) to compute the light-scattering properties of the ND particles, and a code developed by Zubko et al. (2010) for the light-scattering properties of the GRS and AD particles. We average the scattering properties of each test particle category either over different orientations or different particle realizations as summarized in Table 2.

3.2. Size distribution

We test different particle size distributions using truncated power-law distributions ($n(x) \propto x^{-\nu}$) with indices from $\nu = 2.5$ to $\nu = 5.5$. Scattering properties depend on a scatterer's size relative to the incident wavelength. Therefore, instead of the absolute size, we utilize size parameters $x = kr$, where the wave number $k = 2\pi/\lambda$ and r is the radius of a volume-equivalent (subscript "ve") or circumscribing (subscript "cs") sphere. Our range of size parameters extends from $x_{cs,min} = 0.5$ up to $x_{cs,max} = 15$ with equal step sizes of $\Delta x_{cs} = 0.5$. In order to balance the choice between a sufficiently fine step size for the size parameters but also saving computation time, we interpolate some of the scattering-matrix element values when using larger size parameters. The size limits convert to $r_{cs,min} = 1$ cm and $r_{cs,max} = 30$ cm using $\lambda = 12.6$ cm, and $r_{cs,min} = 0.28$ cm and $r_{cs,max} = 8.45$ cm using $\lambda = 3.55$ cm, respectively. The factor x_{cs}/x_{ve} depends on the particle shape; it is 0.610 for ND particles, 0.518 for GRS particles, and 0.612 for AD particles.

We note that the minimum and maximum particle size do not represent physical limits of particle sizes in the coma but the range of particle sizes to which radar wavelengths are the most sensitive. In the case of 73P, there is likely a moderate number of fragments that are larger than the S-band wavelength. However, the ability of the S- and X-band radar measurements to distinguish very large particle sizes is limited to a certain level that appears as a saturation level when analyzing the change of scattering properties as a function of size parameter (see Section 3.4).

3.3. Material

In situ measurements of comets have shown that surfaces of large, intact comets such as 1P/Halley, 19P/Borrelly, and 67P/Churyumov-Gerasimenko do not have a significant abundance of visible water ice on the surface (Belton, 2010; Capaccioni et al., 2015). The mass ratio of refractory materials to volatiles in the near-surface of the nucleus is currently estimated to be about 3–6 around perihelion (Fulle et al., 2010, 2016b; Rotundi et al., 2015).

Villanueva et al. (2006) investigated the composition of fragments C and B in early April of 2006 at IR wavelengths using high-dispersion echelle spectroscopy. Both fragments were depleted in ethane, and fragment C was depleted in most forms of volatile carbon. Fragment C showed a severe depletion of CH_3OH but a common abundance of HCN. Dello Russo et al. (2007) also report depletion of all measured volatile species in respect to H_2O, except for HCN. Therefore, the fraction of refractory materials to volatiles could be higher on both fragments than in comets in average.

Warren (2008) report a constant real part of relative refractive index (Re(m_r)) of 1.7861 for solid water ice at −7 °C at wavelengths from 5 mm to 2 m. The imaginary part (directly related to the conduction and therefore absorption properties) decreases from 3.574×10^{-4} at 1.9-cm wavelength (15.78 GHz) to 0.936×10^{-4} at 14-cm wavelengths (2.14 GHz). Campbell and Ulrichs (1969) report electric permittivities at 450 MHz and 35 GHz for several rocks and minerals collected from various locations on Earth, which provides us with constraints to possible refractive properties of refractory (non-volatile) materials that could appear in comets. Rhyolitic or semi-welded tuff and volcanic ashes have Re(m_r) from 1.6 to 1.9, which are comparable to that of solid ice. Peridotites and obsidian have Re(m_r) ranging from 2.3 to 2.7, and basalts from 2.6 to 3.1. Based on results reported by Fulle et al. (2016a), centimeter-scale pebbles in the cometary comae have porosities of about 52%. Porosity can decrease the effective refractive index critically. Campbell and Ulrichs (1969) also show that in powdered form most rocks and minerals have Re(m_r) of 1.4. Therefore, different mixes of ice and refractory materials with a porosity of 40–60% can lead to a number of possible effective refractive indices.

Brouet et al. (2015) have conducted extensive laboratory measurements of the electric permittivity of cometary material at microwave and radio frequencies (90 MHz–190 GHz). They demonstrate how temperature, porosity, and impurities in the ice affect the refractive index so that the porosity has an inverse correlation with both parts of the refractive index, whereas temperature and volume fraction of non-volatiles have a positive correlation. Typical real parts of the electric permittivities for ice-free dust mantle with a porosity of 50% in a temperature of 113 K vary from 2.39 (Re(m_r) = 1.55, 90 MHz) to about 3.16 (Re(m_r) = 1.78, 190 GHz, interpolated from the reported values), and the imaginary part has an upper limit of 0.035 (Im(m_r) = 0.01, 190 GHz). With varying dust-to-ice ratio (D/I), at a temperature of 110 K, a porosity of 50%, and using frequency of 90 MHz, the real parts of the electric permittivities vary from 2.13 (m_r = 1.46, D/I = 0.1) to 2.34 (m_r = 1.53, D/I = 1.5). The imaginary part is not reported.

In this paper, we use an effective refractive index of $m_r = 1.78 + 0.001i$, which would be equivalent to, e.g., a refractive index of $2.43 + 0.002i$ for "dust", and a refractive index of $1.786 + 0.0001i$ for ice, D/I = 5, and a porosity of 40%. Using a porosity of 52%, the refractive index of the dust would be $2.83 + 0.003i$. The refractive index of the dust depends on its packing density, which we cannot know for certain. However, knowing the exact physical parameters is not critical to the results. Fig. 5 illustrates that μ_C is not very sensitive to small differences in the refractive index; in this case we compare the μ_C of ND particle using $m_r = 1.85 + 0.007i$ to that computed using $m_r = 1.78 + 0.001i$ and find differences in μ_C up to 10%. See further details on how we computed the data in the graph in Section 3.4.

3.4. Search for optimal PSD parameters

In order to model the radar cross section density or the circular-polarization ratio as a function of Doppler shift (Δf), we fit an exponential function to the measured Doppler spectra in each polarization as shown in Fig. 6 to derive the circular-polarization ratio:

$$\mu_C(\Delta f) = \frac{K_{SC}}{K_{OC}} e^{(Q_{SC}-Q_{OC})\Delta f} = K_1 e^{Q_1 \Delta f}. \quad (3)$$

where $K_1 = K_{SC}/K_{OC}$ and $Q_1 = Q_{SC} - Q_{OC}$. Note that the model parameters are different on each side of the nucleus. On the left side

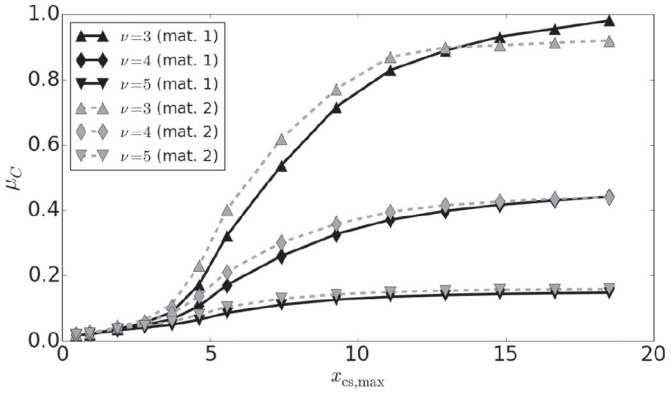

Fig. 5. Comparison between the circular polarization ratios as a function of maximum particle size computed using ND particles with $m_r = 1.78 + 0.001i$ (mat. 1) or $m_r = 1.85 + 0.007i$ (mat. 2) demonstrates the modest effect of choosing a slightly different refractive index.

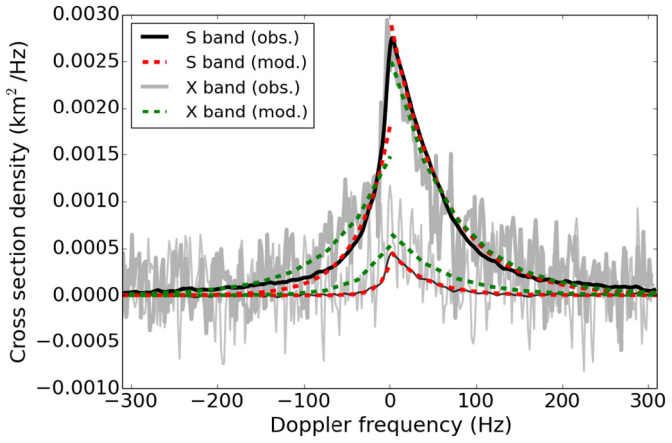

Fig. 6. The radar cross section densities in the OC (thick lines) and SC polarizations (thin lines) as functions of Doppler shift using S-band (black lines) and X-band measurements (gray lines) with fitted models (dashed red and green lines, respectively) that follow $K_{pp}\exp(Q_{pp}\Delta f)$, where the subscript pp refers to either the OC or the SC polarization as relevant. The X-band Doppler spectrum has been scaled to equal the frequency channel width and the wavelength of the S-band Doppler spectrum. (For interpretation of the references to color in this figure legend, the reader is referred to the web version of this article.)

(negative Doppler shift), $K_1 = 0.17$ and $Q_1 = 0.051$ using S band and $K_1 = 0.35$ and $Q_1 = 0.015$ using X band, while on the right side (positive Doppler shift), $K_1 = 0.16$ and $Q_1 = -0.0086$ using S band and $K_1 = 0.26$ and $Q_1 = -0.0021$ using X band.

Once we have an empirical model for the circular polarization ratios as a function of Doppler shift for both S- and X-band observations, we can begin to search for the optimal maximum particle sizes and PSD power-law indices at each different Doppler shift value. We conduct this modeling in two steps: 1. Generating the simulated data of single-particle scattering properties, and 2. deriving empirical equations to model the simulated data from step 1 for further use.

For the first step, we simulate single scattering by irregular particles using discrete-dipole approximation codes (Draine and Flatau, 1994; Zubko et al., 2007; Yurkin and Hoekstra, 2011), which have been developed specifically for this purpose. The codes compute a 4×4 scattering matrix, $\mathbf{F}(\theta)$ (where the scattering angle θ is the angle between the direction of propagation of the incident signal and the observer), and scattering and absorption cross sections that can be utilized to derive the desired radar scattering properties (Bohren and Huffman, 1983). Here we only consider the scattering matrix in the backscattering direction, $\mathbf{F}(180^\circ)$, which is the only relevant direction in monostatic radar measurements.

We derive a weighted average for each radar quantity to account for the size distribution using the following equations:

$$\langle\sigma_{OC}\rangle = \frac{2\pi}{k^2}\frac{\sum_{xmin}^{xmax}(F_{11}(x) - F_{44}(x))n(x)}{\sum_{xmin}^{xmax} n(x)}, \quad (4)$$

$$\langle\sigma_{SC}\rangle = \frac{2\pi}{k^2}\frac{\sum_{xmin}^{xmax}(F_{11}(x) + F_{44}(x))n(x)}{\sum_{xmin}^{xmax} n(x)}, \quad (5)$$

$$\langle\mu_C\rangle = \frac{\sum_{xmin}^{xmax}(F_{11}(x) + F_{44}(x))n(x)}{\sum_{xmin}^{xmax}(F_{11}(x) - F_{44}(x))n(x)}. \quad (6)$$

For the second step, we fit an exponential model to the simulated circular-polarization ratios of the particles as a function of the maximum particle size:

$$\mu_C(r_{max}) = C_1[1 - \exp(C_2(kr_{max})^{C_3})]. \quad (7)$$

The parameters C_1, C_2, and C_3 depend on the particle morphology, particle material, and the PSD power-law index. We determined this function to be the most convenient model for interpolating between the computed values of $\mu_C(r_{max})$. Because the nature of the function is, in fact, cumulative, more complex functions could model $\mu_C(r_{max})$ more accurately. However, this simplified equation is sufficient for the scope of this paper.

Fig. 7 shows the role that the maximum particle size and the power-law index play in the simulated data. This shows that an ambiguity exists between the maximum particle size and the power-law index in terms of interpreting the circular-polarization ratio correctly; for example, $\mu_C = 0.1$ can result from various combinations of ν and r_{max}. Therefore observations at two different wavelengths are critical to pin down both parameters.

We search for the minimum difference between the observational and simulated models simultaneously at two wavelengths, only changing k to determine the wavelength. We discretize the observational model to 60 steps at both positive and negative Doppler shifts, beginning from -120 Hz and ending at 180 Hz, which we considered the range of main interest based on the Doppler spectra. At each step, we search for the optimal maximum particle size from 1 to 20 cm with a step size of 2 mm and an optimal power-law index from 2.51 to 5.50 with a step size of 0.01. Once we find the best-fitting values, we use the corresponding radar cross sections (simulated $\langle\sigma_{eff}\rangle$ and observed σ_{obs}) to compute further physical parameters of the coma, such as an estimate of the number of contributing particles:

$$N_p = \frac{\langle\sigma_{eff}\rangle}{\sigma_{obs}}. \quad (8)$$

Fig. 8 illustrates how a specific pair of measured S- and X-band circular-polarization ratios give the maximum particle size and the PSD power-law index, here, using the total circular polarization ratios for fragment B on May 14 as an example pair of values. Using AD particles, the optimal $\nu = 4.38 \pm 0.05$ and the optimal $r_{cs,max} = 21.8 \pm 0.2$ cm when $\mu_C = 0.309$ in X-band observations and 0.272 in S-band observations with an uncertainty of about 5% for the polarization ratios. Change in the observed μ_C suggests change in either one or both of the maximum particle size and the PSD power-law index. If only the number of particles changes as a function of distance, then μ_C would remain constant.

4. The inferred properties of the coma

4.1. The size distribution as a function of Doppler shift

Fig. 9 illustrates how $r_{cs,max}$ and ν vary as functions of the Doppler shift. The modest increase of $\nu(\Delta f)$ and steep decrease of $r(\Delta f)$ near $\Delta f = 0$ Hz implies decrease of relative fraction of large particles. On

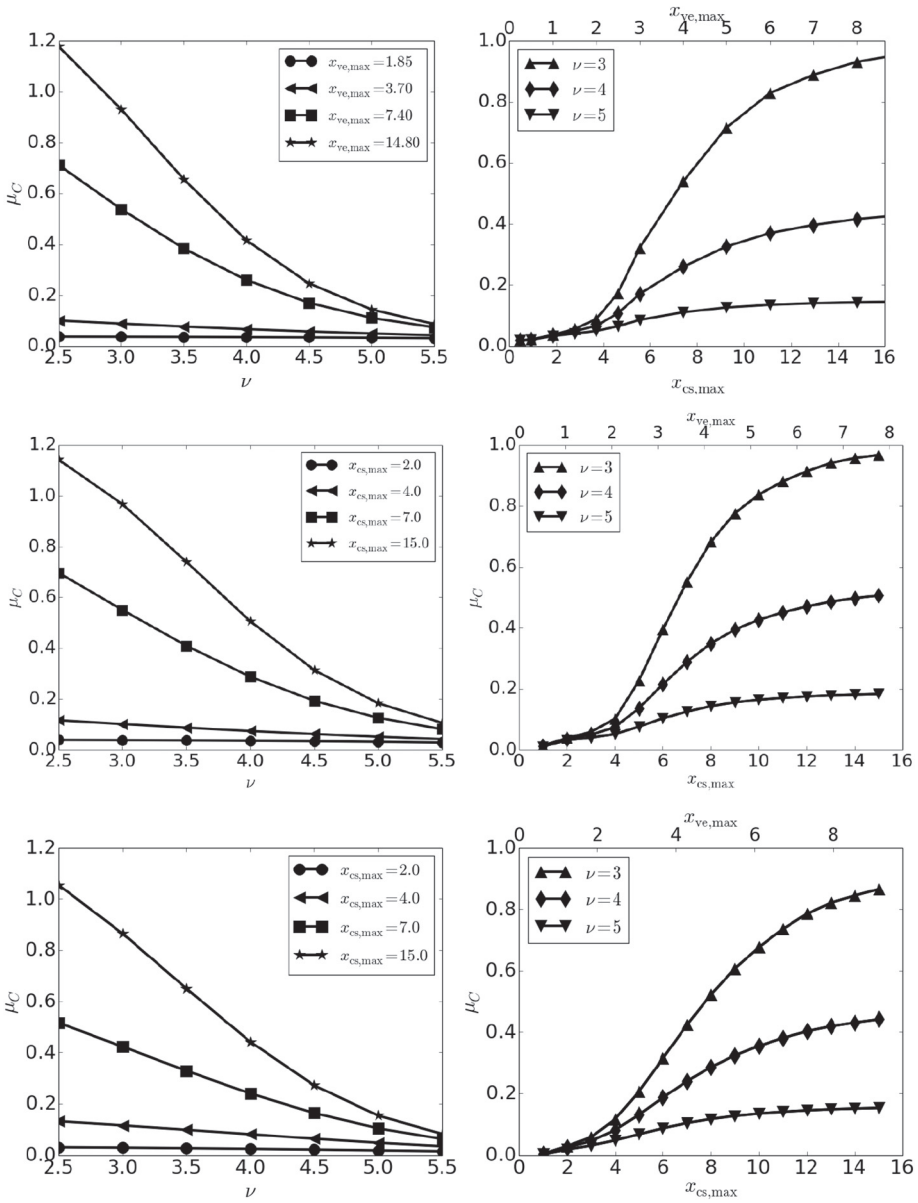

Fig. 7. The effective circular polarization ratio as a function of different power-law size distributions (on the left) or different maximum particle-size parameters (on the right) when using ND (on the top), GRS (in the middle), or AD particles (on the bottom).

May 14th, the Sun-target-observer angle of fragment B is about 93°, which orients the direction of the solar radiation pressure to a nearly right angle to the line of sight. Therefore, we would not expect much difference between the measured radial velocities of particles on the sunward and the tailward sides. However, $\nu(\Delta f)$ shows very different profiles for positive and negative Doppler shift values, which might be caused by noise in the data distorting the observation model on one side by chance or, in fact, reveal clues to the coma PSD on the different sides of the nucleus. The saw edge profile at the lowest Doppler shift values is caused by the boundaries that we set for the range of power-law indices to be tested, but also by the fact that the observed circular-polarization ratios at S band approach zero, which can make the interpretation of the values ambiguous.

There is little difference between the maximum particle sizes derived for the different particle morphologies: For the ND particles $r_{cs,max}$ = 14.4 cm, for the GRS particles $r_{cs,max}$ = 15.0 cm, and for the AD particles $r_{cs,max}$ = 14.5 cm. The difference of the ND particles and the other two morphologies could be caused by different averaging over sizes and orientations, or the effect of particles' surface roughness on the polarization ratio, which is utilized to derive the particle size. Differences between the codes that compute the scattering properties of the particles are an unlikely cause, because both codes that we use have been validated (Zubko et al., 2007).

The weak dependence of the circular polarization ratio to the morphology, when a wide range of particle sizes is considered, is further confirmed by comparative analysis between our work and results from related work by Dogra et al. (2017) using another type of compact irregularly shaped particles, the so-called random Gaussian field particles. The power-law index is greater than the majority of literature estimates for micrometer-scale grains of comets, as reviewed in the Introduction. This supports the assumption that one power-law index does not cover the full PSD from the micron-scale to meter-scale particles, and the power-law index is higher for centimeter-to-decimeter-scale particles.

4.2. The volume of contributing particles

A proper understanding of the particle size distribution can also

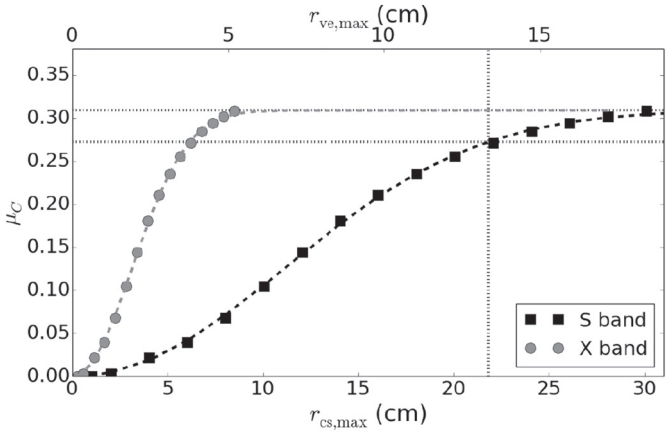

Fig. 8. An example of finding the maximum particle size (spotted vertical line) using the observed total circular-polarization ratios at S-band and X-band for fragment B on May 14th (spotted horizontal lines): If the observed $\mu_C = 0.309$ using X band and $\mu_C = 0.272$ using S band, the optimal $\nu = 4.38 \pm 0.05$ and the optimal $r_{cs,max} = (21.8 \pm 0.2)$ cm. The markers show the simulated circular-polarization ratios using AD particles, and the dashed lines are the fitted curves for each set (black for S band, gray for X band, Eq. (7)).

help us to derive the volume of the large particles contributing to the radar echo. This study alone is not sufficient to reliably estimate the mass loss rate due to the limitations of particle sizes that radar wavelengths are able to detect. Estimation of the PSD power-law index and number of sub-cm particles will require other methods. Also, because the solar radiation pressure has a greater effect on the smaller particles than the larger particles, there exists a non-zero probability that the large particles fall back on the nucleus. We can, however, estimate the number of large particles in the coma with a specific average velocity and evaluate them relative to the comet's escape velocity.

Table 3 lists the number of contributing particles (within the defined size and Doppler shift ranges) estimated for selected observation days. The uncertainty of the observed radar cross sections, which is estimated to be 25% for systematic errors, should be considered in these estimates, because the listed values are directly proportional to the observed radar cross sections. Also, as we underline in this paper, one wavelength cannot fully constrain all PSD parameters due to the ambiguity between the particle size range and distribution form (power-law index). Therefore, if observations at only one wavelength are available, we assume a constant PSD power-law index and the maximum particle size based on the day with observations at both S and X band (May 14) and let the number of particles vary.

Table 3
Estimates of the numbers of contributing particles in the comae of Comet 73P fragments B and C (column 1) for selected days in May 2006 (column 2) simulated using ND particles, GRS particles, or AD particles, respectively (column 3).

Fragm.	Date	N_p (10^{10}, ND | GRS | AD)
B	May 13	5.79 | 8.20 | 4.20
B	May 14	5.17 | 7.34 | 3.75
B	May 15	5.60 | 7.95 | 4.07
B	May 17	4.65 | 6.60 | 3.40
B	May 20	4.04 | 5.74 | 2.95
C	May 07	6.03 | 8.50 | 4.15
C	May 11	3.77 | 5.33 | 2.68
C	May 12	4.05 | 5.73 | 2.90
C	May 13	3.82 | 5.41 | 2.77
C	May 15	4.77 | 6.75 | 3.45
C	May 17	4.90 | 6.95 | 3.58

The total volume of the contributing particles depends strongly on how $r_{ve,min}$ is determined. As discussed by Harmon et al. (1989, 2004) and Campbell et al. (1989), the effective particle size should be at least a few millimeters. Here, we define $r_{ve,min}$ to be the smallest simulated particle size minus one half of the size parameter step size of each PSD, that is, about 3 mm. This gives an expected particle size

$$E(r_{ve}) = \frac{1-\nu}{2-\nu}\frac{r_{ve,min}^{2-\nu} - r_{ve,max}^{2-\nu}}{r_{ve,min}^{1-\nu} - r_{ve,max}^{1-\nu}}, \quad (9)$$

which would result in numerical values from 3.7 to 5.2 mm depending on the particle morphology and the Doppler shift. Using the particle volumes derived from the expected radii and the total number of contributing particles at each considered Doppler shift channel, we can derive a total volume equal to that of a cube with each side of 14–17 m. The number is quite large relative to the sizes of the nuclei, but sensible considering the fracturing state of the comet. However, we stress that it is speculative in terms of the expected particle size, which is why we only present general estimates rather than day-to-day values. Particles that are smaller than 3 mm can constitute a significant fraction of the mass loss. However, we cannot obtain sufficient information on them based on radar observations.

The total mass (M) also depends on the assumed particle density (ρ):

$$M = \rho N_p V_{exp}, \quad (10)$$

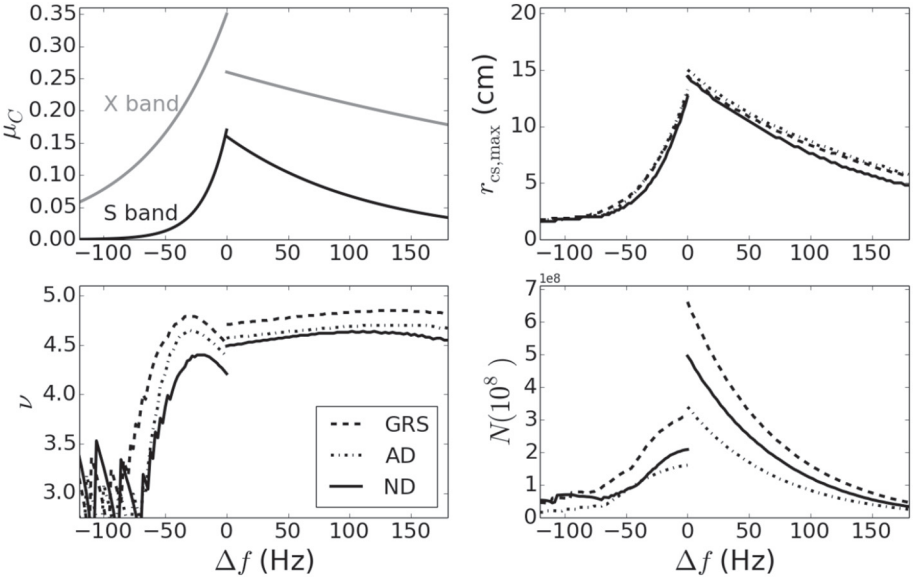

Fig. 9. On the top left, the circular polarization ratio (the black line depicting S-band measurements and the gray line X-band measurements); on the top right, the maximum particle radius; on the bottom left, the PSD power-law index; and on the bottom right, the number of particles, each as a function of Doppler shift for fragment B on May 14th derived from the dual-wavelength radar observations.

where $V_{r,exp}$ is the volume of a particle with an expected size. The average density of the coma particles is assumed to be approximately 600 kg/m^3. Pätzold et al. (2016) report an average density of 533 ± 6 kg/m^3 for 67P/Churyumov-Gerasimenko based on measurements by the Rosetta spacecraft, but especially in the case of a fragmented nucleus, the bulk density of fragmented particles is to some extent higher than the total density of a multi-kilometer-size nucleus due to a lower number of macropores. Here, the mass derived from the total volume varies from 4×10^6 to 30×10^6 kg depending on the day and particle type.

Another notable issue that could affect the speculated number of contributing particles are the particles traveling in the direction perpendicular to the line of sight. When the phase angle of the comet is approximately 90°, solar radiation pressure could align particle propagation so that their radial velocity as detected from the Earth is near 0°, which corresponds to Doppler shift of 0 Hz. Accumulation of echo power by the coma particles at 0 Hz can become indistinguishable from the echo of the nucleus. However, we do not see a significant decrease or shift in the shape of the Doppler spectrum of the coma as the phase angle approaches 90° on May 13 (as shown in Fig. 3 and Table 1), which is consistent with the analysis of Reach et al. (2009) on the modest role that the solar radiation pressure plays in the velocities of large particles compared to the role of the ejection speed due to fragmentation.

4.3. Escaping particles

How significant fraction of the large particles are likely to escape the nucleus? Instead of Doppler shift, we could use the relative radial velocity of the particles with respect to the Earth:

$$v_r = \frac{\lambda \Delta f}{2}. \tag{11}$$

For example, if the nucleus is centered at $\Delta f = 0$ Hz, the radial velocity of the particles relative to that of the nucleus would be 6.3 m/s at 100 Hz using S band. However, we prefer to use Doppler shift here in order to avoid confusion with absolute particle velocities.

The escape velocity on the surface of the nucleus is

$$v_e = \sqrt{\frac{8\pi R_n^2 G\rho}{3}}, \tag{12}$$

where R_n is the sphere-equivalent radius of the nucleus (estimated here to be 400 m for fragment B and 1000 m for fragment C), G is the gravitational constant, and ρ is the density. Using Eq. (11) and $\lambda = 0.126$ m, the surface escape velocity corresponds to Doppler shifts of 4.2 Hz for fragment B and 10.6 Hz for fragment C. The Doppler shift follows from the radial component of a particle's velocity vector, and therefore the particle's velocity can be greater than the Doppler shift suggests. If the observed Doppler shift of a particle is greater than the escape velocity, it escapes the nucleus with a very high probability. This shows that although there is likely a small fraction of particles that might fall back onto the nucleus, the majority of the large coma particles drift away with velocities that are greater than the escape velocity.

4.4. On multiple scattering

For simplicity, we only consider single scattering in all our computations. However, the abundance of multiple scattering between the particles in the coma is worth discussing, because multiple scattering increases especially the echo power in the SC polarization as opposed to single scattering. We can compute an estimate of the number fraction occupied by the contributing large coma particles using N_p and the total volume of the coma (V_{coma}):

$$f_V = \frac{N_p}{V_{coma}} \tag{13}$$

If we estimate the contributing particles to be located within a 5-km radius from the nucleus during the time of the observation, we find an average number fraction of 0.1 particles per m^3. This strongly supports the negligible amount of multiple scattering between the centimeter-to-decimeter-scale particles. Multiple scattering is most likely very near the nucleus where the particle density is greatest. However, any potential second-order scattering in that region likely contributes only to a negligible fraction of the measured total echo power.

5. Conclusions

We present a new method to study the particle size distribution and size range of centimeter-to-decimeter-scale coma particles using dual-wavelength radar observations. As an example case, we use radar observations of the comae of fragments B and C of Comet 73P/Schwassmann-Wachmann 3, although the method can be utilized to analyze any comet with a radar-detectable echo.

Our results are fairly consistent with the existing literature on coma particle size distributions: The PSD power-law index is long known from *in situ* studies of stable short-period comets to be steeper for large chunks than small grains, and comet 73P presumably obeys the same trend despite its actively occurring disintegration. We find that using dual-wavelength radar observations, power-law indices from 4.0 to 4.8 fit to the observed polarization ratios, the value depending on the particle shape and distance from the nucleus. The particle sizes follow this size distribution from approximately mm-scale up to major-axis diameters of approximately 30 cm. We find a more modest rate of change of the PSD power-law index as a function of Doppler shift at positive Doppler shift values than at negative Doppler shift values, indicating different coma dynamics on sunward and tailward sides of the nucleus.

The observed circular polarization ratio as a function of Doppler shift reveals that particle sizes increase progressively closer to the nucleus. The difference between the maximum particle sizes derived using different particle morphologies is relatively small despite the noticeable difference in their appearance (radii 14.5–17.8 cm). Therefore, we can conclude that the shape does not play a very critical role, as long as a wide range of sizes is included and the model particles have non-spherical morphologies.

We also confirm earlier findings by Howell et al. (2007) that the particle number density decreases as the Doppler shift increases. This shows that the observed particle velocity increase is directly proportional to the distance from the nucleus, which supports the results by, e.g., Reach et al. (2009) that smaller particles get accelerated by forces such as the solar radiation pressure and rocket forces caused by ice sublimation, whereas major fragments are dominated by the ejection speed from the fragmentation process. Regardless of the small role of accelerating forces, we show that even the cm-to-dm-scale particles are more likely to escape the nucleus than to fall back.

Acknowledgments

This research was supported by NASA's Near-Earth Object Observations Program through grant no. NNX13AQ46G awarded to Universities Space Research Association (USRA) for the Arecibo Planetary Radar Program, and after April 2018 through grant no. 80NSSC18K1098 awarded to the University of Central Florida. The Arecibo Observatory is a National Science Foundation facility operated under cooperative agreement by University of Central Florida, Yang Enterprises, Inc., and Universidad Ana G. Mendez. During the time of the observations, the facility was operated by the Cornell University.

References

Belton, M.J.S., 2010. Cometary activity, active areas, and a mechanism for collimated outflows on 1P, 9P, 19P, and 81P. Icarus 210, 881–897. https://doi.org/10.1016/j.

icarus.2010.07.007. Dec.
Bohren, C.F., Huffman, D.R., 1983. Absorption and Scattering of Light by Small Particles. ISBN 0-471-05772-X. John Wiley & Sons, Inc., USA.
Brouet, Y., Levasseur-Regourd, A.C., Sabouroux, P., Encrenaz, P., Thomas, N., Heggy, E., Kofman, W., 2015. Permittivity measurements of porous matter in support of investigations of the surface and interior of 67P/Churyumov-Gerasimenko. Astron. Astrophys. 583 A39.
Brownlee, D., Tsou, P., Aléon, J., Alexander, C.M.O., Araki, T., Bajt, S., Baratta, G.A., Bastien, R., Bland, P., Bleuet, P., Borg, J., Bradley, J.P., Brearley, A., Brenker, F., Brennan, S., Bridges, J.C., Browning, N.D., Brucato, J.R., Bullock, E., Burchell, M.J., Busemann, H., Butterworth, A., Chaussidon, M., Cheuvront, A., Chi, M., Cintala, M.J., Clark, B.C., Clemett, S.J., Cody, G., Colangeli, L., Cooper, G., Cordier, P., Daghlian, C., Dai, Z., D'Hendecourt, L., Djouadi, Z., Dominguez, G., Duxbury, T., Dworkin, J.P., Ebel, D.S., Economou, T.E., Fakra, S., Fairey, S.A.J., Fallon, S., Ferrini, G., Ferroir, T., Fleckenstein, H., Floss, C., Flynn, G., Franchi, I.A., Fries, M., Gainsforth, Z., Gallien, J.-P., Genge, M., Gilles, M.K., Gillet, P., Gilmour, J., Glavin, D.P., Gounelle, M., Grady, M.M., Graham, G.A., Grant, P.G., Green, S.F., Grossemy, F., Grossman, L., Grossman, J.N., Guan, Y., Hagiya, K., Harvey, R., Heck, P., Herzog, G.F., Hoppe, P., Hörz, F., Huth, J., Hutcheon, I.D., Ignatyev, K., Ishii, H., Ito, M., Jacob, D., Jacobsen, C., Jacobsen, S., Jones, S., Joswiak, D., Jurewicz, A., Kearsley, A.T., Keller, L.P., Khodja, H., Kilcoyne, A.L.D., Kissel, J., Krot, A., Langenhorst, F., Lanzirotti, A., Le, L., Leshin, L.A., Leitner, J., Lemelle, L., Leroux, H., Liu, M.-C., Luening, K., Lyon, I., MacPherson, G., Marcus, M.A., Marhas, K., Marty, B., Matrajt, G., McKeegan, K., Meibom, A., Mennella, V., Messenger, K., Messenger, S., Mikouchi, T., Mostefaoui, S., Nakamura, T., Nakano, T., Newville, M., Nittler, L.R., Ohnishi, I., Ohsumi, K., Okudaira, K., Papanastassiou, D.A., Palma, R., Palumbo, M.E., Pepin, R.O., Perkins, D., Perronnet, M., Pianetta, P., Rao, W., Rietmeijer, F.J.M., Robert, F., Rost, D., Rotundi, A., Ryan, R., Sandford, S.A., Schwandt, C.S., See, T.H., Schlutter, D., Sheffield-Parker, J., Simionovici, A., Simon, S., Sitnitsky, I., Snead, C.J., Spencer, M.K., Stadermann, F.J., Steele, A., Stephan, T., Stroud, R., Susini, J., Sutton, S.R., Suzuki, Y., Taheri, M., Taylor, S., Teslich, N., Tomeoka, K., Tomioka, N., Toppani, A., Trigo-Rodríguez, J.M., Troadec, D., Tsuchiyama, A., Tuzzolino, A.J., Tyliszczak, T., Uesugi, K., Velbel, M., Vellenga, J., Vicenzi, E., Vincze, L., Warren, J., Weber, I., Weisberg, M., Westphal, A.J., Wirick, S., Wooden, D., Wopenka, B., Wozniakiewicz, P., Wright, I., Yabuta, H., Yano, H., Young, E.D., Zare, R.N., Zega, T., Ziegler, K., Zimmerman, L., Zinner, E., Zolensky, M., 2006. Comet 81P/Wild 2 under a microscope. Science 314, 1711. https://doi.org/10.1126/science.1135840. Dec.
Busemann, H., Nguyen, A.N., Cody, G.D., Hoppe, P., Kilcoyne, A.L.D., Stroud, R.M., Zega, T.J., Nittler, L.R., 2009. Ultra-primitive interplanetary dust particles from the comet 26P/Grigg-Skjellerup dust stream collection. Earth Planet. Sci. Lett. 288, 44–57. https://doi.org/10.1016/j.epsl.2009.09.007. Oct.
Campbell, D.B., Harmon, J.K., Shapiro, I.I., 1989. Radar observations of Comet Halley. Astrophys. J. 338, 1094–1105. https://doi.org/10.1086/167259. Mar.
Campbell, M.J., Ulrichs, J., 1969. Electrical properties of rocks and their significance for lunar radar observations. J. Geophys. Res. 74, 5867–5881.
Capaccioni, F., Coradini, A., Filacchione, G., Erard, S., Arnold, G., Drossart, P., De Sanctis, M.C., Bockelee-Morvan, D., Capria, M.T., Tosi, F., Leyrat, C., Schmitt, B., Quirico, E., Cerroni, P., Mennella, V., Raponi, A., Ciarniello, M., McCord, T., Moroz, L., Palomba, E., Ammannito, E., Barucci, M.A., Bellucci, G., Benkhoff, J., Bibring, J.P., Blanco, A., Blecka, M., Carlson, R., Carsenty, U., Colangeli, L., Combes, M., Combi, M., Crovisier, J., Encrenaz, T., Federico, C., Fink, U., Fonti, S., Ip, W.H., Irwin, P., Jaumann, R., Kuehrt, E., Langevin, Y., Magni, G., Mottola, S., Orofino, V., Palumbo, P., Piccioni, G., Schade, U., Taylor, F., Tiphene, D., Tozzi, G.P., Beck, P., Biver, N., Bonal, L., Combe, J.-P., Despan, D., Flamini, E., Fornasier, S., Frigeri, A., Grassi, D., Gudipati, M., Longobardo, A., Markus, K., Merlin, F., Orosei, R., Rinaldi, G., Stephan, K., Cartacci, M., Cicchetti, A., Giuppi, S., Hello, Y., Henry, F., Jacquinod, S., Noschese, R., Peter, G., Politi, R., Reess, J.M., Semery, A., 2015. The organic-rich surface of comet 67P/Churyumov-Gerasimenko as seen by VIRTIS/Rosetta. Science 347 (1) aaa0628.
Dello Russo, N., Vervack, R.J., Weaver, H.A., Biver, N., Bockelée-Morvan, D., Crovisier, J., Lisse, C.M., 2007. Compositional homogeneity in the fragmented comet 73P/Schwassmann-Wachmann 3. Nature 448, 172–175 July.
Dogra, S., Grynko, Y., Zubko, E., Förstner, J., 2017. Radar backscattering from a large-grain cometary coma: numerical simulation. Astron. Astrophys. 608https://doi.org/10.1051/0004-6361/201730801. A20, Nov.
Draine, B.T., Flatau, P.J., 1994. Discrete-dipole approximation for scattering calculations. J. Opt. Soc. Am. A 11, 1491–1499.
Fulle, M., Colangeli, L., Agarwal, J., Aronica, A., Della Corte, V., Esposito, F., Grün, E., Ishiguro, M., Ligustri, R., Lopez Moreno, J.J., Mazzotta Epifani, E., Milani, G., Moreno, F., Palumbo, P., Rodríguez Gómez, J., Rotundi, A., 2010. Comet 67P/Churyumov-Gerasimenko: the GIADA dust environment model of the Rosetta mission target. Astron. Astrophys. 522 A63, Nov.
Fulle, M., Della Corte, V., Rotundi, A., Rietmeijer, F.J.M., Green, S.F., Weissman, P., Accolla, M., Colangeli, L., Ferrari, M., Ivanovski, S., Lopez-Moreno, J.J., Epifani, E.M., Morales, R., Ortiz, J.L., Palomba, E., Palumbo, P., Rodriguez, J., Sordini, R., Zakharov, V., 2016a. Comet 67P/Churyumov-Gerasimenko preserved the pebbles that formed planetesimals. Mon. Not. R. Astron. Soc. 462, S132–S137 Nov.
Fulle, M., Marzari, F., Della Corte, V., Fornasier, S., Sierks, H., Rotundi, A., Barbieri, C., Lamy, P.L., Rodrigo, R., Koschny, D., Rickman, H., Keller, H.U., López-Moreno, J.J., Accolla, M., Agarwal, J., A'Hearn, M.F., Altobelli, N., Barucci, M.A., Bertaux, J.-L., Bertini, I., Bodewits, D., Bussoletti, E., Colangeli, L., Cosi, M., Cremonese, G., Crifo, J.-F., Da Deppo, V., Davidsson, B., Debei, S., De Cecco, M., Esposito, F., Ferrari, M., Giovane, F., Gustafson, B., Green, S.F., Groussin, O., Grün, E., Gutierrez, P., Güttler, C., Herranz, M.L., Hviid, S.F., Ip, W., Ivanovski, S.L., Jerónimo, J.M., Jorda, L., Knollenberg, J., Kramm, R., Kührt, E., Küppers, M., Lara, L., Lazzarin, M., Leese, M.R., López-Jiménez, A.C., Lucarelli, F., Mazzotta Epifani, E., McDonnell, J.A.M., Mennella, V., Molina, A., Morales, R., Moreno, F., Mottola, S., Naletto, G., Oklay, N., Ortiz, J.L., Palomba, E., Palumbo, P., Perrin, J.-M., Rietmeijer, F.J.M., Rodríguez, J., Sordini, R., Thomas, N., Tubiana, C., Vincent, J.-B., Weissman, P., Wenzel, K.-P., Zakharov, V., Zarnecki, J.C., 2016b. Evolution of the dust size distribution of Comet 67P/Churyumov-Gerasimenko from 2.2 au to Perihelion. Astrophys. J. 821 Apr.
Harmon, J.K., Campbell, D.B., Hine, A.A., Shapiro, I.I., Marsden, B.G., 1989. Radar observations of Comet IRAS-Araki-Alcock 1983d. Astrophys. J. 338, 1071–1093.
Harmon, J.K., Nolan, M.C., Ostro, S.J., Campbell, D.B., 2004. Radar studies of comet nuclei and grain comae. In: Festou, M.C., Keller, H.U., Weaver, H.A. (Eds.), Comets II. Univ. of Arizona Press, Arizona, USA, pp. 265–279.
Hilchenbach, M., Kissel, J., Langevin, Y., Briois, C., von Hoerner, H., Koch, A., Schulz, R., Silén, J., Altwegg, K., Colangeli, L., Cottin, H., Engrand, C., Fischer, H., Glasmachers, A., Grün, E., Haerendel, G., Henkel, H., Höfner, H., Hornung, K., Jessberger, E.K., Lehto, H., Lehto, K., Raulin, F., Le Roy, L., Rynö, J., Steiger, W., Stephan, T., Thirkell, L., Thomas, R., Torkar, K., Varmuza, K., Wanczek, K.-P., Altobelli, N., Baklouti, D., Bardyn, A., Fray, N., Krüger, H., Ligier, N., Lin, Z., Martin, P., Merouane, S., Orthous-Daunay, F.R., Paquette, J., Revillet, C., Siljeström, S., Stenzel, O., Zaprudin, B., 2016. Comet 67P/Churyumov-Gerasimenko: close-up on dust particle fragments. Astrophys. J. Lett. 816https://doi.org/10.3847/2041-8205/816/2/L32. L32, Jan.
Howell, E.S., Nolan, M.C., Harmon, J.K., Lovell, A.J., Benner, L.A., Ostro, S.J., Campbell, D.B., Margot, J., 2007. Radar and Radio Observations of the Fragmented Comet 73P/Schwassmann-Wachmann3. In: AAS/Division for Planetary Sciences Meeting Abstracts #39. Bulletin of the American Astronomical Society, vol. 39. pp. 486 Oct.
Kelley, M.S., Reach, W.T., Lien, D.J., 2008. The dust trail of Comet 67P/Churyumov Gerasimenko. Icarus 193, 572–587. https://doi.org/10.1016/j.icarus.2007.08.018. Feb.
Kemppinen, O., Nousiainen, T., Lindqvist, H., 2015. The impact of surface roughness on scattering by realistically shaped wavelength-scale dust particles. J. Quant. Spectrosc. Radiat. Transf. 150, 55–67. https://doi.org/10.1016/j.jqsrt.2014.05.024. Jan.
Langevin, Y., Hilchenbach, M., Ligier, N., Merouane, S., Hornung, K., Engrand, C., Schulz, R., Kissel, J., Rynö, J., Eng, P., 2016. Typology of dust particles collected by the COSIMA mass spectrometer in the inner coma of 67P/Churyumov Gerasimenko. Icarus 271, 76–97 June.
Lindqvist, H., Jokinen, O., Kandler, K., Scheuvens, D., Nousiainen, T., 2014. Single scattering by realistic, inhomogeneous mineral dust particles with stereogrammetric shapes. Atmos. Chem. Phys. 14, 143–157.
Mazets, E.P., Aptekar, R.L., Golenetskii, S.V., Guryan, Y.A., Dyachkov, A.V., Ilyinskii, V.N., Panov, V.N., Petrov, G.G., Savvin, A.V., Sagdeev, R.Z., Sokolov, I.A., Khavenson, N.G., Shapiro, V.D., Shevchenko, V.I., 1986. Comet Halley dust environment from SP-2 detector measurements. Nature 321, 276–278. https://doi.org/10.1038/321276a0. May.
Muinonen, K., Nousiainen, T., Fast, P., Lumme, K., Peltoniemi, J., 1996. Light scattering by Gaussian random particles: ray optics approximation. J. Quant. Spectrosc. Radiat. Transf. 55, 577–601.
Naidu, S.P., Benner, L.A.M., Margot, J.-L., Busch, M.W., Taylor, P.A., 2016. Capabilities of Earth-based radar facilities for near-Earth asteroid observations. Astron. J. 152 99, Oct.
Nolan, M.C., Harmon, J.K., Howell, E.S., Benner, L.A., Giorgini, J.D., Ostro, S.J., Campbell, D.B., Margot, J.L., 2006. Radar observations of Comet 73P/Schwassmann-Wachmann 3. In: AAS/Division for Planetary Sciences Meeting Abstracts #38. Bulletin of the American Astronomical Society. vol. 38. pp. 504 Sept.
Ostro, S.J., 1993. Planetary radar astronomy. Rev. Mod. Phys. 65, 1235–1295.
Pätzold, M., Andert, T., Hahn, M., Asmar, S.W., Barriot, J.-P., Bird, M.K., Häusler, B., Peter, K., Tellmann, S., Grün, E., Weissman, P.R., Sierks, H., Jorda, L., Gaskell, R., Preusker, F., Scholten, F., 2016. A homogeneous nucleus for comet 67P/Churyumov-Gerasimenko from its gravity field. Nature 530, 63–65. https://doi.org/10.1038/nature16535. Feb.
Price, M.C., Kearsley, A.T., Burchell, M.J., Hörz, F., Borg, J., Bridges, J.C., Cole, M.J., Floss, C., Graham, G., Green, S.F., Hoppe, P., Leroux, H., Marhas, K.K., Park, N., Stroud, R., Stadermann, F.J., Telisch, N., Wozniakiewicz, P.J., 2010. Comet 81P/Wild 2: the size distribution of finer (sub-10 μm) dust collected by the Stardust spacecraft. Meteorit. Planet. Sci. 45, 1409–1428. https://doi.org/10.1111/j.1945-5100.2010.01104.x. Sept.
Reach, W.T., Vaubaillon, J., Kelley, M.S., Lisse, C.M., Sykes, M.V., 2009. Distribution and properties of fragments and debris from the split Comet 73P/Schwassmann-Wachmann 3 as revealed by Spitzer Space Telescope. Icarus 203, 571–588 Oct.
Rotundi, A., Sierks, H., Della Corte, V., Fulle, M., Gutierrez, P.J., Lara, L., Barbieri, C., Lamy, P.L., Rodrigo, R., Koschny, D., Rickman, H., Keller, H.U., López-Moreno, J.J., Accolla, M., Agarwal, J., A'Hearn, M.F., Altobelli, N., Angrilli, F., Barucci, M.A., Bertaux, J.-L., Bertini, I., Bodewits, D., Bussoletti, E., Colangeli, L., Cosi, M., Cremonese, G., Crifo, J.-F., Da Deppo, V., Davidsson, B., Debei, S., De Cecco, M., Esposito, F., Ferrari, M., Fornasier, S., Giovane, F., Gustafson, B., Green, S.F., Groussin, O., Grün, E., Güttler, C., Herranz, M.L., Hviid, S.F., Ip, W., Ivanovski, S., Jerónimo, J.M., Jorda, L., Knollenberg, J., Kramm, R., Kührt, E., Küppers, M., Lazzarin, M., Leese, M.R., López-Jiménez, A.C., Lucarelli, F., Lowry, S.C., Marzari, F., Epifani, E.M., McDonnell, J.A.M., Mennella, V., Michalik, H., Molina, A., Morales, R., Moreno, F., Mottola, S., Naletto, G., Oklay, N., Ortiz, J.L., Palomba, E., Palumbo, P., Perrin, J.-M., Rodríguez, J., Sabau, L., Snodgrass, C., Sordini, R., Thomas, N., Tubiana, C., Vincent, J.-B., Weissman, P., Wenzel, K.-P., Zakharov, V., Zarnecki, J.C., 2015. Dust measurements in the coma of comet 67P/Churyumov-Gerasimenko inbound to the Sun. Science 347 (1) aaa3905, Jan.
Tuzzolino, A.J., Economou, T.E., Clark, B.C., Tsou, P., Brownlee, D.E., Green, S.F., McDonnell, J.A.M., McBride, N., Colwell, M.T.S.H., 2004. Dust measurements in the coma of Comet 81P/Wild 2 by the dust flux monitor instrument. Science 304, 1776–1780. https://doi.org/10.1126/science.1098759. June.
Villanueva, G.L., Bonev, B.P., Mumma, M.J., Magee-Sauer, K., DiSanti, M.A., Salyk, C., Blake, G.A., 2006. The volatile composition of the split ecliptic comet 73P/

Schwassmann-Wachmann 3: a comparison of fragments C and B. Astrophys. J. Lett. 650, L87–L90 Oct.
Virkki, A., Muinonen, K., 2016. Radar scattering by planetary surfaces modeled with laboratory-characterized particles. Icarus 269, 38–49.
Warren, S.G., 2008. Optical constants of ice from the ultraviolet to the microwave: a revised compilation. J. Geophys. Res. 113, D14220.
Weaver, H.A., Lisse, C.M., Mutchler, M.J., Lamy, P., Toth, I., Reach, W.T., 2006. Hubble Space Telescope Investigation of the Disintegration of 73P/Schwassmann-Wachmann 3. In: AAS/Division for Planetary Sciences Meeting Abstracts #38. Bulletin of the American Astronomical Society. vol. 38. pp. 490 Sept.
Yurkin, M.A., Hoekstra, A.G., 2011. The discrete-dipole-approximation code ADDA: capabilities and known limitations. J. Quant. Spectrosc. Radiat. Transf. 112, 2234–2247.
Zubko, E., Muinonen, K., Shkuratov, Y., Videen, G., Nousiainen, T., 2007. Scattering of light by roughened Gaussian random particles. J. Quant. Spectrosc. Radiat. Transf. 106, 604–615.
Zubko, E., Petrov, D., Grynko, Y., Shkuratov, Y., Okamoto, H., Muinonen, K., Nousiainen, T., Kimura, H., Yamamoto, T., Videen, G., 2010. Validity criteria of the discrete dipole approximation. Appl. Opt. 49, 1267. https://doi.org/10.1364/AO.49.001267. Mar.
Zubko, E., Shkuratov, Y., Mishchenko, M., Videen, G., 2008. Light scattering in a finite multi-particle system. J. Quant. Spectrosc. Radiat. Transf. 109, 2195–2206. https://doi.org/10.1016/j.jqsrt.2008.03.007. Aug.
Zubko, E., Shkuratov, Y., Videen, G., 2015. Effect of morphology on light scattering by agglomerates. J. Quant. Spectrosc. Radiat. Transf. 150, 42–54. https://doi.org/10.1016/j.jqsrt.2014.06.023. Jan.
Zubko, E., Videen, G., Hines, D.C., Shkuratov, Y., 2016. The positive-polarization of cometary comae. Planet. Space Sci. 123, 63–76. https://doi.org/10.1016/j.pss.2015.09.020. Apr.